Fusion Engineering and Design 202 (2024) 114415

Contents lists available at ScienceDirect

Fusion Engineering and Design

journal homepage: www.elsevier.com/locate/fusengdes

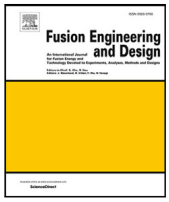

Computational Thermal-Fluid Dynamics analyses of borated water distribution in the Vacuum Vessel of the Divertor Tokamak Test facility

Roberto Bonifetto [a,*], Gianluca Barone [b,c], Mauro Dalla Palma [d,e], Antonio Froio [a], Emanuela Martelli [b], Federico Vair [a], Roberto Zanino [a], Andrea Zappatore [a]

[a] NEMO group, Dipartimento Energia "Galileo Ferraris", Politecnico di Torino, Corso Duca degli Abruzzi, 24, Torino, 10129, Italy
[b] ENEA, Department of Fusion and Nuclear Safety Technology, Frascati, 00044, RM, Italy
[c] DTT S.c. a r.l., Frascati, 00044, RM, Italy
[d] Consorzio RFX, Padova, 35127, Italy
[e] Istituto per la Scienza e Tecnologia dei Plasmi, Consiglio Nazionale delle Ricerche, Padova, 35127, Italy

ARTICLE INFO

Keywords:
DTT
Vacuum vessel
CFD
Thermal-hydraulics
Tokamak

ABSTRACT

This work presents the full set of 3D Computational Thermal-Fluid Dynamics (CFD) analyses of the Divertor Tokamak Test (DTT) Vacuum Vessel (VV). The VV D-shaped double shell structure, divided into 18 *Regular* and *Special* sectors, is actively maintained at the operating temperature of 60 °C by borated water in forced flow to counteract the thermal loads and the heat transfer with the surroundings. Due to manufacturing and integration constraints, the different sectors cannot share the same design: the water will flow in the free space between the two shells composing the VV but, given the complexity of the geometry, a careful hydraulic design is mandatory, to avoid local stagnation points which may cause either overheating or freezing. The different hydraulic paths are separately analysed with the Star-CCM+ software, with a SST $k-\omega$ turbulence closure, proving the effectiveness of their design (pressure drop, temperature constraints and stagnation/backflow). In addition, the borated water mass flow rate distribution among the different paths is assessed. To conclude, results from CFD analyses are exploited to approximate the hydraulic characteristic of each sector and to develop a system-level model of the full VV with the Modelica language. The overall VV pressure drop of $\Delta p = 2810$ Pa, the outlet mixing temperature of $T_{out,mix} = 333.06$ K and a mass flow rate distribution close to the homogeneous condition (≈ 2.22 kg s^{-1} in each sector) confirm that no relevant issues are found in the current VV design from the thermal-hydraulic point of view.

1. Introduction

1.1. Divertor tokamak test

One of the major challenges encountered in the magnetic confinement of high temperature plasmas is the so-called heat exhaust and impurities control issue [1]. By trusting current extrapolations on scrape-off layer (SOL) power decay length λ_q [2], the heat fluxes foreseen for the European DEMO will be absolutely untolerable by current divertor configurations based on active cooling only. The *Divertor Tokamak Test* (DTT) facility, currently under construction at the Enea Frascati research centre in Italy [3,4], has to integrate different aspects to recreate, at least in terms of dimensionless quantities, the operating conditions planned for DEMO, while ensuring wide flexibility to test different magnetic divertor topologies, plasma facing materials and alternative plasma shape configurations to bring an integrated solution for the power exhaust issue by 2030 [5].

1.2. DTT vacuum vessel

The VV in a Tokamak system is designed to provide an enclosed environment where favourable conditions for a burning plasma can be reached (i.e high quality vacuum). The VV design however has to take into account several other requirements besides the high quality vacuum: it also provides support for in-vessel components (e.g first wall, breeding blanket) while withstanding nuclear and radiative loads. In addition to that, the VV has a shielding function towards Toroidal Field (TF) coils and it represents a first confinement barrier, in case of accidents, between plasma and external environment.

* Corresponding author.
E-mail address: roberto.bonifetto@polito.it (R. Bonifetto).
URL: https://www.nemo.polito.it (R. Bonifetto).

https://doi.org/10.1016/j.fusengdes.2024.114415
Received 13 October 2023; Received in revised form 29 March 2024; Accepted 1 April 2024
Available online 10 April 2024

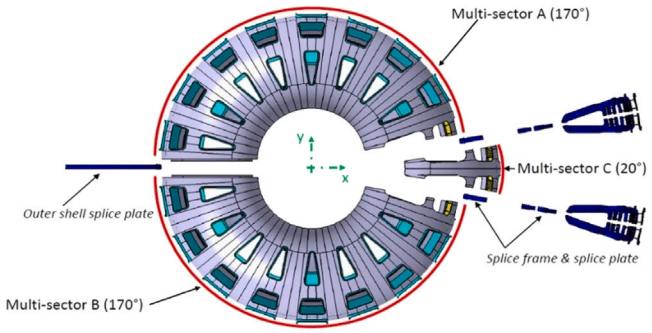

Fig. 1. DTT Vacuum Vessel multi-sectors assembling and manufacturing strategy. *Source:* Courtesy of ENEA.

Table 1
CVs main characteristics.

CV	Inlet	Volume [m^3]	Irradiated surface[a] [m^2]
1	R/L	0.697	5.56
2	R/L	0.693	5.43
3	R/L	0.697	5.55
4	L	0.692	5.50
5	L	0.702	5.62
6	L	0.761	5.89
7	R	0.825	6.11
8	L	0.763	5.79
9	R	0.690	5.55
10	L	0.688	5.51
11	R	0.670	5.53
12	L	0.687	5.40

[a] The outer irradiated surface is needed to estimate the total power deposition and the outlet temperature (see Section 5).

The DTT vacuum vessel consists of a D-shaped double shell toroidal structure (outboard diameter of 6960 mm, inboard diameter of 2530 mm and total height of 3910 mm) with a total number of 82 access ports that will be exploited for diagnostics/control and maintenance of in-vessel components. The VV will be manufactured in three main sections only, called respectively *multi-sector A*, *B* and *C*: the two 170° multi-sectors (*A* and *B*) will be built, assembled and tested (inter-shell pressurization test with water at $p_{test} = 7$ bar) separately and then connected, to fully complete the toroidal geometry, with the last 20° section *C* (with the TF coil already mounted), as shown in Fig. 1. Splice plates are employed to connect adjacent multi-sectors, and they are directly welded on site, while splice frames instead allow an easier integration of the access ports.

From the structural point of view, the VV can be split into 18 reference geometries (sectors) with 20° toroidal development. The VV will be subjected to a static and uniform radiative heat load of $-70\ \mathrm{W\,m^{-2}}$ from the Thermal Shield (TS). The negative sign highlights that the radiative load to the TS is a heat sink for the VV. The nuclear load, mainly due to D–D reactions [5], instead, will be pulsed: 8.84 kW spread over the entire vessel for a max of 85 s over 3600 s duty cycle, resulting in ≈ 12 W average heat flux over each 20° sector (Double Null scenario [6]). Therefore, the nuclear heat load is neglected in present, steady state analyses.

Borated water (0.8 wt%, 95% ^{10}B enriched), which controls the temperature and acts as neutron shield, flows in the ≈ 13.5 m^3 volume between inner and outer VV shells. A set of poloidal and toroidal ribs, exploited to sustain and to give stiffness to the overall structure, creates complex internal flow paths for the coolant. The total mass flow rate of 20 $\mathrm{kg\,s^{-1}}$ is fed from the bottom via 9 inlets and flows mainly from bottom to top (in view of the limited number of connections in the toroidal directions), where it is collected by 9 outlets, staggered with respect to the inlet.

The scope of the work is to understand, by means of detailed numerical simulations with the commercial software Star-CCM+ [7], if the current VV design satisfies a series of qualitative design requirements (DRs):

- DR1: The borated water must not go below a minimum temperature of $T_{min} = 313.15$ K causing possible boron precipitation, with consequent deposition and formation of encrustations over the VV components, that can damage the structure and partially or even totally occlude passages for the flow.
- DR2: The borated water must not overcome a maximum temperature of $T_{max} = 353.15$ K, which would accelerate the steel corrosion.
- DR3: The VV must be fully drainable from borated water to allow baking.

One of the key output expected from the TH analyses is the indication of how the borated water is distributed between the different available paths inside each CV: macroscopic flow imbalances between the IB/OB legs, or local imbalances among the parallel paths of same leg, have to be avoided as much as possible to homogenize VV pressure and temperature fields.

In the next sections, the logic behind the setup of the numerical analyses carried out to assess the first two points is presented, while the last DR was used as a driver for the present VV design and is therefore satisfied by definition.

2. Computational domain

The minimum control volume (CV) that has to be simulated consists in two-half adjacent sectors, still with 20° toroidal development, completely independent from a hydraulic point of view with respect to adjacent CVs except for inlet and outlet pipes, where the weak pressure coupling has been neglected as a first approximation (*I Modelling Assumption*). Therefore, within the 18 sectors a total number of 12 CVs can be extracted and separately analysed to fully characterize the VV, see Fig. 2. A further distinction can be done between *Regular* and *Special* CVs. The former are characterized by three specific geometries (CV1, CV2, and CV3 highlighted in red, orange and yellow respectively in Fig. 2 for better visualization) which are repeated multiple times in the VV geometry, typically with a mirrored symmetry. Therefore, if CV1-type R (inlet on the right-end side) is simulated, then the solution of CV1-type L is automatically defined by mirroring that solution. The *Special* ones instead are one-of-a-kind, namely they appear in the VV geometry only once. Special CVs include splice plates (CV4), splice frames (CV10-11-12) and skewed (to allow for the Neutral Beam Injection system) or missing ports (CV8-9 and CV6-7 respectively). For convention, "*Regular*" and/or "*Special*" CVs sharing the same inlet pipe are grouped in the same hydraulic sector *i*#.

As a *II Modelling Assumption*, only the fluid volume has been modelled, without the inclusion of solid walls (shells, pipes and ribs) neglecting therefore the conjugate heat transfer nature of the problem. This reduces the simulation complexity while producing a conservative estimation of the temperature field, since hot/cold temperature spots will not be smoothed out by diffusion in the solids. Key info of extracted fluid volumes are quantitatively summarized in Table 1.

By focusing the attention on the CV, the fluid entering from the bottom is split by an inlet distribution chamber between the inboard (IB) and outboard (OB) legs, which are hydraulically independent except for inlet and outlet regions (Fig. 3(a)) .

The inlet distribution chamber can have from two (Fig. 3(b)) to three (Fig. 3(c)) apertures, which will have an effect on the computed pressure drop (see Section 4). Inside each leg, the coolant mass flow is further divided into three major parallel paths (Fig. 4): at the OB leg, the presence of connecting holes in the poloidal ribs allows an exchange of mass among the three channels in the core of the CV. From

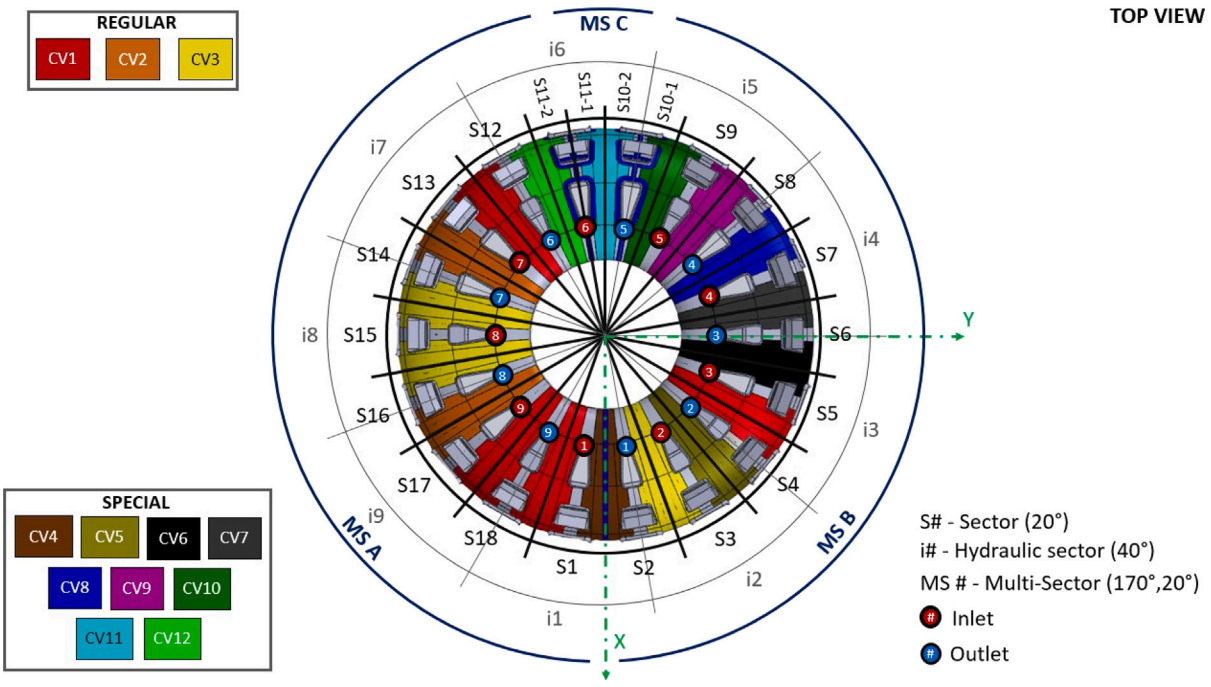

Fig. 2. Full VV nomenclature for TH analyses; *Regular* and *Special* sectors and CVs are identified and grouped in hydraulic sectors.

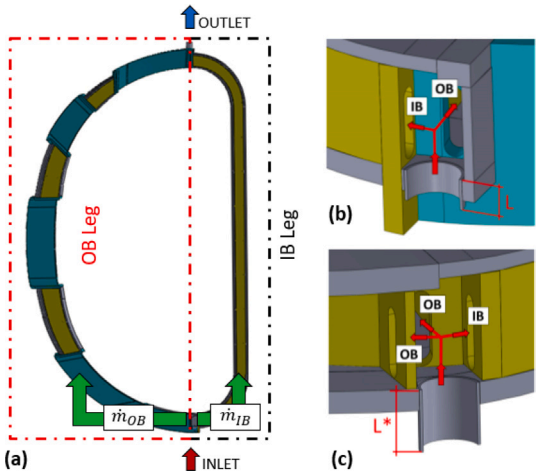

Fig. 3. (a) CV lateral view with IB and OB legs distinction. Two-way (b) and three-way (c) inlet distribution chambers, with inlet pipe lengths $L = 32$ mm and $L^* = 65$ mm. Note how only half of the inlet belongs to each CV.

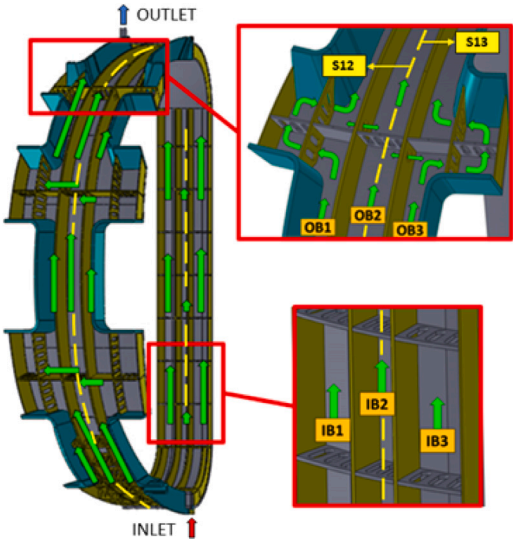

Fig. 4. Zoom on OB and IB parallel channels, for a regular CV1, showing the staggered inlet and outlet and the CV division between two adjacent sectors (S12 and S13 according to the nomenclature in Fig. 2). The length of the green arrows already provide a quantitative representation of the mass flow rate distribution in each channel. See Section 4 for details.

a practical point of view it means that the mass flow rate flowing in the first channel (OB1) at the bottom of the CV is generally different from the one that flows at the top of the same channel. For what concerns the IB leg, instead, the flow is still distributed in three parallel channels but, in view of the lack of holes in the poloidal ribs, they are hydraulically independent (except at the bottom and top).

For the sake of completeness, special CVs 10, 11 and 12 have additional IB paths.

3. Simulation setup

3.1. Models and closures

In view of the complex geometry of the VV, a broad range of characteristic lengths and velocity scales are expected. If the attention is focused at the inlet region however, the estimation of the Reynolds number suggests a turbulent regime (laminar to turbulent transition at Re ≈ 2300):

$$\mathrm{Re} = \frac{\rho u D}{\mu} = \frac{4\dot{m}_{inlet}}{\mu \pi D} \approx 88000, \tag{1}$$

where $D = 54.76$ mm is the inlet pipe diameter, $\dot{m}_{inlet} = 2.22\ \mathrm{kg\,s^{-1}}$ is the inlet mass flow rate in each CV (see Section 3.4 dedicated to boundary conditions) and $\mu = 5.8613 \cdot 10^{-4}\ \mathrm{Pa\,s^{-1}}$ is the dynamic viscosity of borated water (see Section 3.5 dedicated to material properties characterization).

The bidirectional link between mean flow properties and turbulence is taken into account with a RANS SST $k-\omega$ model [8], combined with an *all* y^+ wall treatment, in view of three main considerations:

1. Better prediction of the heat transfer coefficient in stagnation regions, where the $k-\varepsilon$ is known to overestimate the turbulence providing non conservative solutions.
2. Reduced computational cost with respect to more complex and expensive turbulence closures as the seven equations Reynolds Stress Transport model.
3. The Menter's SST $k-\omega$ combined with an *all* y^+ treatment is the recommended choice by Star-CCM+ among $k-\omega$ models [9].

Additionally, as well as already introduced (see Section 2), hypotheses and *modelling assumptions* for the thermal-hydraulic (TH) simulations are grouped below, and will be discussed further in this work:

I Neglect existing pressure coupling between adjacent CVs.
II Model, discretize and solve equations for the fluid volume only (no conjugate heat transfer).
III Assume homogeneous mass flow repartition among the 9 inlets ($2.22\ \mathrm{kg\,s^{-1}}$) and in turn in the adjacent CVs ($1.11\ \mathrm{kg\,s^{-1}}$, as each inlet is split in two equal halves between adjacent CVs).

The *I Modelling Assumption* is necessary since, otherwise, the VV should have been modelled as a whole entity, leading to unbearable computational efforts; this assumption is considered reasonable as the coupling is limited to a very small portion of the domain (less than 1%). Nevertheless, the validity of this approach is verified *a posteriori* with a system-level modelling (see Section 5). Concerning the *II Modelling Assumption*, as mentioned in Section 2, it is a conservative assumption, which allows reducing significantly the computational cost. Finally, the *III Modelling Assumption* is required because of the *I Modelling Assumption*, and it is also verified *a posteriori* with a system-level model (see Section 5).

The flow is incompressible (Mach number evaluated at the inlet $\mathrm{Ma} = 6\cdot10^{-3}$, much lower than 0.3), while material properties are assumed to be constant (no pressure/temperature dependence); only the density variation with temperature is relevant, as it would induce body forces (natural circulation). This is however modelled with the Boussinesq approximation, as explained in Section 3.2.

3.2. Buoyancy and gravity contribution

Despite the VV hydraulic circuit being a closed loop, the effect of gravity must be included because, due to the TS negative radiative load acting on the outer wall of the VV, the borated water will cool down, with consequent variations of the density. Density gradients, in gravitational fields, result in modified body forces which could be the driver of natural convective flows inside the VV: since they actively participate to the energy exchange, they should be correctly captured by the model.

The possibility of including density gradients and thus buoyancy forces actually goes against the initial hypothesis of incompressible flow: in this cases to enhance the convergence of the simulation while limiting as much as possible the complexity of the model, the Boussinesq model can be exploited. It must be stressed that the Boussinesq approximation is valid only for small temperature differences and thus density variations, and that the coefficient β_v must be taken from appropriate tables of thermo-physical properties. As far as the first warning is concerned, it has been computed that the surface integral over the regular sector outer wall of the TS radiative load of $-70\ \mathrm{W\,m^{-2}}$ results in a total power of $\Phi \approx 395$ W. If a mass flow rate of $\dot{m} = 1.11\ \mathrm{kg\,s^{-1}}$ of borated water with specific heat $c = 4019.68\ \mathrm{J\,kg^{-1}\,K^{-1}}$ (see Section 3.5) is considered, and the contribution of pressure is neglected, from the first law of thermodynamics between inlet ("in") and outlet ("out") sections it can be derived that:

$$\Delta T = T_{in} - T_{out} = -\frac{\Phi}{\dot{m}c} \approx -\frac{-395}{1.11\cdot 4019.68} \approx 0.09\ \mathrm{K}. \tag{2}$$

If the value of $\beta_v = 5.82\cdot10^{-4}\ \mathrm{K^{-1}}$ is considered (pure water), then the constraint suggested by Star-CCM+ for the Boussinesq approximation validity is largely satisfied:

$$\beta_v \Delta T \approx 5.82\cdot10^{-4}\cdot 0.1 \ll 1. \tag{3}$$

An exploring simulation on regular CV1 allowed to compute a map of the Richardson number Ri, defined as

$$\mathrm{Ri}_k = \frac{g\beta_v\left(\overline{T_k} - T_{min,k}\right)L_{max}}{\overline{u}_k{}^2}, \tag{4}$$

in different cross-sections of the domain, when the effect of buoyancy was captured by the model. The dimensionless number was conservatively approximated by considering the largest equivalent diameter $L_{max} \approx 216$ mm, the difference between minimum and average temperature $\left(\overline{T_k} - T_{min,k}\right)$ over the cross-section k and the average velocity $\overline{u}_k$, always evaluated on the same cross-section.

Values of the approximated Richardson number significantly larger than that suggested from theory ($\mathrm{Ri} = 19$ in the upper region of CV1 OB3 channel with respect to the $\mathrm{Ri} \ll 1$ requirement), confirm the non-negligible influence of buoyancy, which is taken into account in all the numerical solution.

3.3. Solver, time modelling and mesh generation

Since convective flows resulting from density gradients have a remarkable influence on flow properties and distribution, it is generally preferred to exploit a coupled approach rather than a segregated one; the former though is much more computationally expensive. In Star-CCM+ the governing equations (continuity, momentum and energy) are efficiently condensed together and solved once (for more details, see [9]).

As far as the time modelling is concerned, there are no strong indications that the thermal-fluid dynamics solution is unsteady being the forcing functions (negative radiative load from TS) and material properties constant over time. However, due to the complexity of the VV internal structure, a pure steady-state analysis has demonstrated to be unable to capture physical fluctuations of mean flow properties around average values (constant over time). As it will be discussed in the results (Section 4), a steady-state analysis is able to found a steady solution whose main parameters are sufficiently in agreement with those computed by averaging in time the pressure and mass flow rate fluctuations (period $T \approx 3$ s) computed with an implicit time marching scheme ($\Delta t = 0.1$ s). The accuracy sacrifice is largely compensated by the increased speed of the numerical simulations. A conservative *Courant–Friedrichs–Lewy* (CFL) number equal to five has proven to be reliable for the steady simulation (*pseudo-time marching approach*) since, as the mesh refinement increases, the discretized equations become much more sensible to CFL selection, with diverging residual even with the introduction of max/min bounds to the variables. The optimal CFL choice is a function of several parameters as mesh quality and magnitude of the body forces, and there are no general laws to easily identify optimal values: optimized CFL control strategy is far from the scope of this work but it could be considered a priority in the future to speed up thermal-fluid dynamics analyses of possible design updates.

For what concerns the mesh, a polyhedral surface and volumetric mesh has been combined with a prism layer mesh near the wall. An unstructured polyhedral mesh in fact does not guarantee an uniform cell's centroid distance with respect to the wall, and for this reason, when resolving the boundary layer, a prism layer mesh is generally adopted to avoid wrong/poor reconstruction of velocity and temperature gradients by linear interpolation near the wall. In the present work, the SST $k-\omega$ model was adopted with an all y^+ treatment, recommended choice in Star-CCM+. With an *all* y^+ treatment, the centroid of the near wall cell should preferably lay in the viscous sublayer (y^+ order one) or in the log layer ($y^+ > 30$), limiting as much

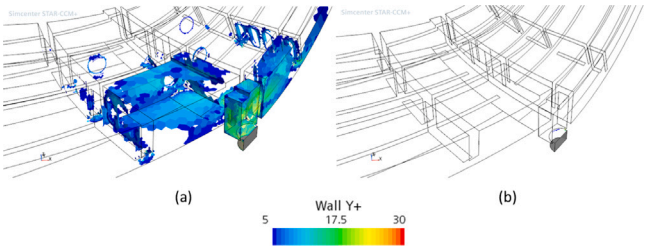

Fig. 5. Comparison between $y_H = 0.5$ mm (a) and $y_H = 0.05$ mm (b) wall y^+ distribution. In (b), the number of cells in the buffer layer are drastically reduced. Acceptable values of $y^+ < 5$ and $y^+ > 30$ are out of the selected scale and therefore they do not appear in the plots.

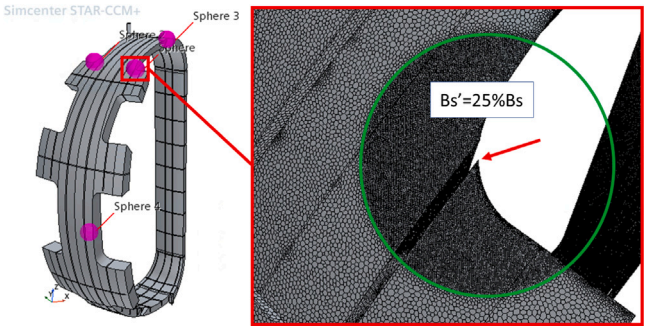

Fig. 6. Geometry and mesh of CV1, with volumetric/surface mesh refinement by means of spheres (in purple) centred on the sharp edges of the fluid geometry (or in general where instabilities occur) indicated by the red arrow, with a zoom on the resulting refined mesh.

as reasonably possible the number of cells in the buffer layer ($1 < y^+ < 30$), where however Star-CCM+ will perform an interpolation to limit the inaccuracy of the result. After a series of explorative runs, an optimized first layer thickness of $y_H = 0.05$ mm provided a reasonable y^+ distribution in inlet and outlet region (see Fig. 5). A total prism layer thickness of $y_T = 2.5$ mm and a total number of prism layers $N = 10$ guarantee a smooth transition between the two meshes, with a stretch factor G lower than 1.5. For more info about the prism layer mesh see [9]. To avoid numerical instabilities when exploiting finer meshes (base size of the order of 15 mm), local volumetric refinements by means of spheres have been adopted. In the region of the mesh intersecated by the sphere, the base size of the surface and volumetric mesh has been reduced to 25% of the original base size, while the number of prism layers has been increased up to 15. A zoom of the mesh refinement is presented in Fig. 6 for the regular CV1. Numerical instabilities have been solved thanks to this refinement.

3.4. Boundary conditions

As already introduced above, in [5] the total mass flow rate in the 18 sectors of the VV is $\dot{m}_{tot} = 20\ \mathrm{kg\,s^{-1}}$. As a first guess (*III Modelling Assumption*), whose goodness must be verified a posteriori by system-level simulations, it is assumed that the total mass flow rate is perfectly distributed among the nine inlet pipes, with a resulting value at each inlet of $\dot{m}_{inlet} = 2.22\ \mathrm{kg\,s^{-1}}$. Moreover, it is also assumed that the mass flow rate of each inlet is equally distributed in the two adjacent CVs: the prescribed mass flow rate in half of the inlet pipe is therefore equal to $\dot{m}_{CV} = 1.11\ \mathrm{kg\,s^{-1}}$. The boundary conditions (BCs) applied can be divided in two families according to the piece of physics that they refer to:

- Hydraulic BCS (see Fig. 7(a)):
  - BC of "*Mass Flow Inlet*" (MFI) type, i.e. a prescribed mass flow rate of $\dot{m}_{CV} = 1.11\ \mathrm{kg\,s^{-1}}$ at half of the inlet pipe.

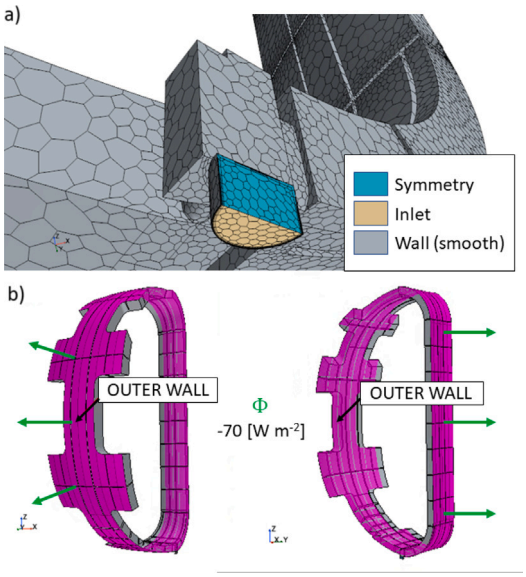

Fig. 7. Zoom on the inlet region of the mesh with different BCs (a) and visualization of the constant and uniform heat flux Φ acting on the outer wall fluid surface (b).

  - BC of "*Pressure Outlet*" type at the outlet section, i.e. uniform $P_{out} = 0$ Pa gauge.
  - BC of "*Wall*" type with "*smooth*" wall surface specification for all the surfaces in contact with the VV structure, i.e. no-slip condition.
  - BC of "*Symmetry Plane*" type for the vertical cross section of inlet/outlet pipes.
- Thermal BCs:
  - Prescribed uniform inlet temperature of $T_{in} = 333.15$ K.
  - Prescribed heat flux of $-70\ \mathrm{W\,m^{-2}}$ as thermal specification for the surfaces of the fluid in contact with the outer wall of the VV (both IB and OB, see Fig. 7(b)).
  - Adiabatic BC for all the remaining surfaces: for the two vertical cross sections of inlet and outlet pipes this condition holds automatically in view of the imposed symmetry condition, see again Fig. 7(a).

3.5. Borated water thermo-physical properties

Besides controlling the temperature, the water flowing in the double-shell D-shaped VV has to provide a neutronic barrier to the ex-vessel components, like the superconducting toroidal field (TF) coils. The thickness of the IB leg is 13 cm (10 cm of borated water) and, because of volume constraints at the inner side of the machine, no neutron shield is attached to the IB rear shell.

The three-dimensional neutronic activation and dose rate analyses for the design and licensing of DTT, and corrosion effect on stainless steel (AISI316L type family) base microstructure as well as welding-induced microstructures of borated water mixture (0.8 wt%, 95% ^{10}B enriched), have been carried out in [10,11], respectively. Such share of boron in water was considered sufficient to satisfy the design requirement during high performance plasma, allowing to limit the heat deposition below 1 $\mathrm{mW\,m^{-3}}$ [5] in TF coils during high-performance operation (maximum $1.5 \cdot 10^{17}$ neutron $\mathrm{s^{-1}}$ 2.5 MeV from D–D reactions and $1.5 \cdot 10^{15}$ neutron $\mathrm{s^{-1}}$ 14 MeV from D–T reactions) while ensuring the integrity of the materials, reducing the so-called stress corrosion cracking (combined effect of corrosion and constant mechanical load).

Table 2
Thermo-physical properties of borated water (60 °C, 4 bar, 0.8 wt%, 95% ^{10}B enriched) exploited for material characterization in TH simulations.

Property	Value
Density[a] [kg m^{-3}] [12]	983.3
Dynamic viscosity [Pa s] [12]	$5.8613 \cdot 10^{-4}$
Specific heat [J kg^{-1} K^{-1}] [13]	4019.68
Thermal conductivity[b] [W m^{-1} K^{-1}] [14]	0.6967
Thermal expansion coefficient[c] [K^{-1}]	$5.82 \cdot 10^{-4}$
Turbulent Prandtl number [–]	0.9

[a] of pure water because negligible difference.
[b] two extrapolations needed to cover DTT VV desired temperature and concentration values.
[c] of pure water because not available for borated water.

Table 3
Grid independence analysis on the prism layer mesh with BS = 15 mm, considering smooth (surface roughness K_s = 0) and rough (K_s = 6.3 μm) surfaces and uniform (MFI)/fully developed (FDI) profiles as inlet specifications.

Mesh	Target y^+	y_H [mm]	N	G	K_s [μm]	BC	Δp [Pa] (% dev.)
Ref	*all* y^+	0.05	10	1.33	Smooth	MFI	2734.8 (0%)
1	*all* y^+	0.05	7	1.65	Smooth	MFI	2705.5 (−1.1%)
2	*low* y^+	0.01	15	1.34	Smooth	MFI	2745.5 (+0.4%)
3	*high* y^+	1	2	1.5	Smooth	MFI	2525.7 (−7.6%)
4	*all* y^+	0.05	10	1.33	Smooth	FDI	2670.4 (−2.4%)
5	*all* y^+	0.05	10	1.33	6.3	FDI	2675.7 (−2.2%)

Correlations on aqueous solutions of boric acid thermo-physical properties with respect to temperature, pressure and boron concentration have been therefore exploited to assess density, dynamic viscosity, specific heat and thermal conductivity of such mixture in the operating range foreseen for DTT VV (60 °C, 4 bar), as summarized in Table 2.

4. Results and discussion

In this section, the most relevant simulation outcomes are presented and discussed. Being the number of computational domains analysed large, this section cannot focus on all the specific details that can be retrieved by high-fidelity CFD simulations. Instead, only few characteristic CVs will be presented and discussed, thanks to the existing similitudes in all CVs geometries and BCs, which allow to extend the simulation setup to the whole VV. Despite that, to present a comprehensive view of the VV, results about all CVs have been included where needed.

4.1. Pressure drop

The CV pressure drop has been defined as the difference between surface average absolute pressure at inlet and outlet sections. From this value, the static pressure head of $\rho g \Delta z = 983.3 \cdot 9.81 \cdot 3.905 = 37.7$ kPa is subtracted to retrieve the pressure drop due to friction only. As demonstrated for the regular CV1, the pressure drop is influenced by the refinement of the prism layer mesh. As reported in Table 3, different wall treatments result in deviations which are not always negligible with respect to the reference mesh (≈ 7 million cells, base size BS = 15 mm, first layer thickness y_H = 0.05 mm, total prism layer thickness y_T = 2.5 mm, number of prism layer N = 10, stretch factor G = 1.33, resulting in the best trade-off between accuracy and computational cost), proving that a *high* y^+ treatment leads to a poor estimation of the pressure drop. In mesh number three in fact, pure *high* y^+ approach has been investigated revealing a significant deviation with respect to reference data. In addition, residuals for this attempt are significantly larger. A *high* y^+ wall treatment is therefore not recommended.

The effect of surface roughness on pressure drop has also been assessed on the reference mesh with respect to the original smooth-surface approximation, considering a surface finish of K_s = 6.3 [μm], as reported for the semi-finished products in the provisional document containing technical specification for the VV call for tenders. Moreover, pure hydraulic simulations have been carried out on CV1 inlet (axisymmetric 2D domain) to compute fully developed inlet (FDI) velocity and $k-\omega$ profiles to assess the effect of inlet turbulent specification on the pressure drop, against the initial hypothesis of MFI inlet BC where uniform velocity and $k-\omega$ profiles are prescribed by default (see Table 3 again).

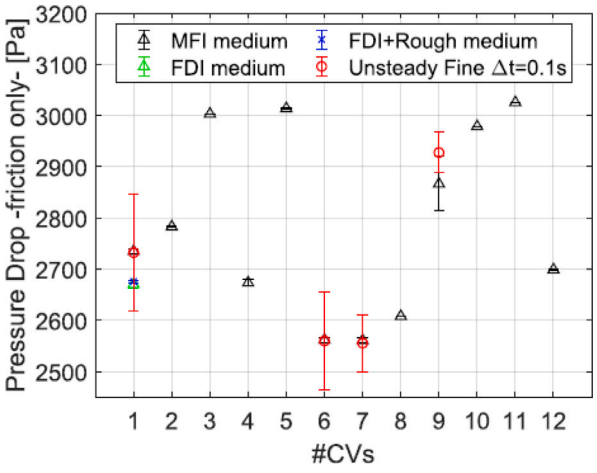

Fig. 8. Pressure drops at nominal mass flow rate (1.11 kg s^{-1}) computed from CFD simulations for the 12 different CVs. MFI stands for "Mass Flow Inlet" while FDI stands for "Fully Developed Inlet". The medium mesh is the reference mesh in Table 3, while the fine mesh has BS = 5 [mm]. The prism layer mesh setup is the same for both.

In absolute terms, pressure drop uncertainties are of the order of ±5 Pa (between *smooth* and *rough* cases), of ±65 Pa between MFI and FDI and ±30 Pa between different prism layer setup. Concerning the comparison between steady-state and transient results, the unsteady simulation with the finest mesh (≈ 22 million cells, BS = 5 mm) shows that reports' fluctuations found with steady solver are actually physical and are even larger than the numerical noise found with pure steady-state simulation. Using the reference mesh instead, a steady-state is reached also with the unsteady solver. For the finest mesh, the pressure drop oscillates with a period of $T \approx 3$ s and an absolute maximum amplitude of 115 Pa around the mean value. IB and OB mass flow rates share the same period, with an absolute amplitude limited to 20 g s^{-1} around the mean value. The deviations between average values found with steady and unsteady approaches are of ~1.2% if the comparison is done for the reference mesh and of ~ 0.16% if the finest mesh is considered.

The above-mentioned information are obtained from CV1 but are valid also for CV6, CV7 and CV9 as well (even if with slightly different values). In all the other CVs, report fluctuations are negligible and the steady solution is clean. Concerning the pressure drop unbalance among the different CVs, the lowest average pressure drop of 2561 ± 56 Pa is found for CV7 (−6.4% w.r.t CV1, the uncertainty comes from unsteady simulation with the finest mesh), while the largest average pressure drop of 3026 ± 115 Pa is found for CV11 (+10.6% w.r.t CV1). The comparison among the pressure drop of the different CVs evaluated with the reference mesh (or with the finest mesh when available) together with the corresponding uncertainties is presented in Fig. 8. The sensitivity to prism layer refinement, inlet turbulent specification and surface characterization can be considered negligible with respect to the uncertainties related to the non perfect steady-state reached by the numerical solution and the Δp differences between CVs, except for the *high* y^+ treatment, that should be avoided.

Pressure drops are coherently mostly localized at inlet and outlet sections, as already found for previous works on ITER VV [15,16]. Larger pressure drops are found for geometries having a three-way inlet

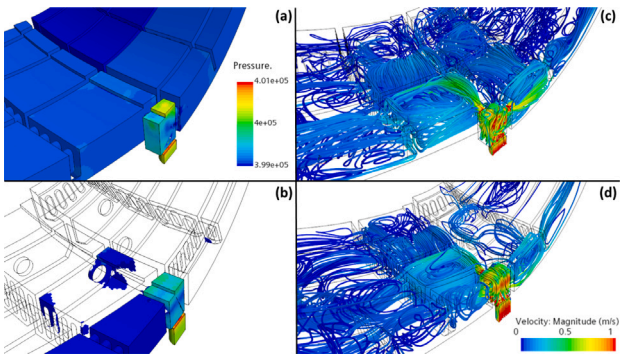

Fig. 9. On the left, comparison between CV1 (a) and CV3 (b) pressure fields at the inlet section. The legend is cropped at 3.99 bar to show that in (b) the coolant enters the core of CV3 domain with a pressure already below that threshold. On the right, streamline comparison of CV1 (c) and CV3 (d) respectively, using inlet surface as source seed with 15 × 15 grid points. Streamline colour is related to the local velocity of the fluid particle following that path.

(CV3, CV5, CV10) rather than a two-way inlet topology, as demonstrated by the pressure field comparison between CV1 and CV3 inlet regions in Fig. 9. The only exception is found for CV11, where the largest pressure drop occurs despite a two-way inlet type because of its geometry significantly different from the others.

4.2. Mass flow rate distribution within the CV and stagnation

Streamlines scenes as those presented in Fig. 10 are useful to visualize the flow path and the main velocity scales involved in the DTT VV. Velocity ranges from peak values of $\approx 1\ \mathrm{m\,s^{-1}}$ at inlet and outlet sections down to average values of $1-10\ \mathrm{cm\,s^{-1}}$ in the core of the domain, requiring deeper investigations to assess the presence and location of possible stagnation regions. To provide a quantitative estimation of the borated water distribution within each CV, the mass flow rate has been evaluated in each channel (three OB channels and three IB channels respectively, except for CV10, CV11 and CV12 where the number of IB channels varies) at three different latitudes via mass flow reports in Star-CCM+, for a total of 18 measurements (see Fig. 11 for details). However this output does not provide a qualitative indication of the flow inside each channel, because the identification of severe recirculation or stagnation zones cannot be immediately retrieved from global information. Therefore, tables of mass flow repartition have been coupled with 2D plots of the velocity component V_s (locally tangent to the orientation of the channel cross section s) at each section, to capture where recirculation was strong. For the top (TOP) and bottom (BM) cross sections, the velocity V_s along direction s was defined as:

$$V_s = \left(\pm u\cos\left(\alpha_i\right) \pm v\cos\left(\beta_i\right)\right)\sin\left(\theta\right) + w\cos\left(\theta\right), \tag{5}$$

being α_i, β_i the complementary angles identifying projection of s on x–y plane, and $\theta_{TOP}, \theta_{BM}$ the relative inclination of s with respect to z-axis.

Concerning the macroscopical mass flow rate repartition between IB and OB legs, all the CVs show that the borated water flows preferably in the OB leg, but overall each CV appears to be sufficiently balanced, as presented in Fig. 12.

The uncertainty derived from the physical fluctuations captured with the steady solver on the finest mesh in CV1 is of the order of $\pm 20\ \mathrm{g\,s^{-1}}$. This value has been extended to all the CVs where detailed unsteady simulations were not performed, relying on the steady state analyses with the standard mesh (Ref. mesh in Table 3) thanks to the grid independence analysis carried out on CV1.

More in detail, in Table 4 the mass flow repartition within CV1 is presented. Despite each CV being different from the others, there are some recurrent aspects in the coolant repartition that can be summarized as:

Table 4
Mass flow rate repartition within CV1 OB and IB channels. Reported mean values are taken from unsteady fine (BS = 5 mm) results. Of the total mass flow rate ($\dot{m}_{TOT}$ = 1.11 $\mathrm{kg\,s^{-1}}$), ≈ 620 $\mathrm{g\,s^{-1}}$ go to the OB leg while remaining ≈ 490 $\mathrm{g\,s^{-1}}$ to the IB leg.

	Mass Flow Rate Fraction [-]			
Channel	Bottom	Equatorial	Up	Tot
OB1	12%	18%	26%	
OB2	24%	24%	21%	56%
OB3	20%	14%	9%	
IB1	21%	21%	21%	
IB2	4%	4%	4%	44%
IB3	19%	19%	19%	
TOT	100%	100%	100%	100%

- The mass flow repartition within the OB leg is characterized by larger flow in the poloidal channel closer to the inlet at the bottom, which progressively shifts to the opposite side when approaching the outlet at the top, where the maximum mass flow rate is instead detected at the OB poloidal channel opposite to the inlet (inlets and outlets are staggered).
- The mass flow repartition within the IB leg is characterized by almost equal flow in lateral channels IB1-IB3 (≈ 20% of total mass flow rate), while only $\approx 2-4\%$ of the borated water flows in the central channel IB2, due to its lower cross-section. In CV4, the presence of the splice plate further shrinks channel IB2, where mass flow rate drops down to 1.5%.

Peculiar IB channels topologies in CV11 and CV12 introduce backflow in portions of those channels. Even if the TH analyses did not spot any relevant issue related to that, simple modifications of the shape/diameter of the holes for the toroidal flow will be discussed in the dedicated Section 6, to solve that not optimal condition.

4.3. Energy balance (outlet temperature)

In Table 1 the outer surface of each fluid volume was reported. Despite small differences among different CVs, the impact on the energy balance is negligible: the average temperature difference between inlet and outlet is ΔT = 0.09 K, with deviations limited to some [mK]. Even in CVs showing some stagnation/backflow, the radiative load of $-70\ \mathrm{W\,m^{-2}}$ coming from the thermal shield does not lead to any violation of the minimum temperature constraint.

5. System-level modelling

Since the CFD simulation of the entire VV might be prohibitive, to reconstruct its global hydraulic behaviour from the separate analyses of the different CVs a system-level model has been used, written in Modelica language and based on the Modelica Standard Library (MSL) and on the (validated) ThermoPower library [17,18]. By considering each CV as a 1D component of this model, the pressure drops due to friction can be approximated as a quadratic function with respect to the mass flow rate. Since the pressure drop is null when no borated water flows in the VV, the operating Δp_{nom} evaluated through CFD analyses at the nominal mass flow rate of $\dot{m}_{inlet} = 1.11\ \mathrm{kg\,s^{-1}}$ can be exploited to approximate the hydraulic behaviour of the CV as:

$$\Delta p = \frac{\Delta p_{nom}}{(\dot{m}_{inlet})^2}\cdot \dot{m}^2 \tag{6}$$

This is clearly an approximation since it does not account for the buoyancy effect (temperature dependent), already proven to be non negligible. However, for small mass flow rate deviations around the nominal value (±10%), the quadratic characteristic has been demonstrated to be sufficiently accurate in the prediction of the Δp when

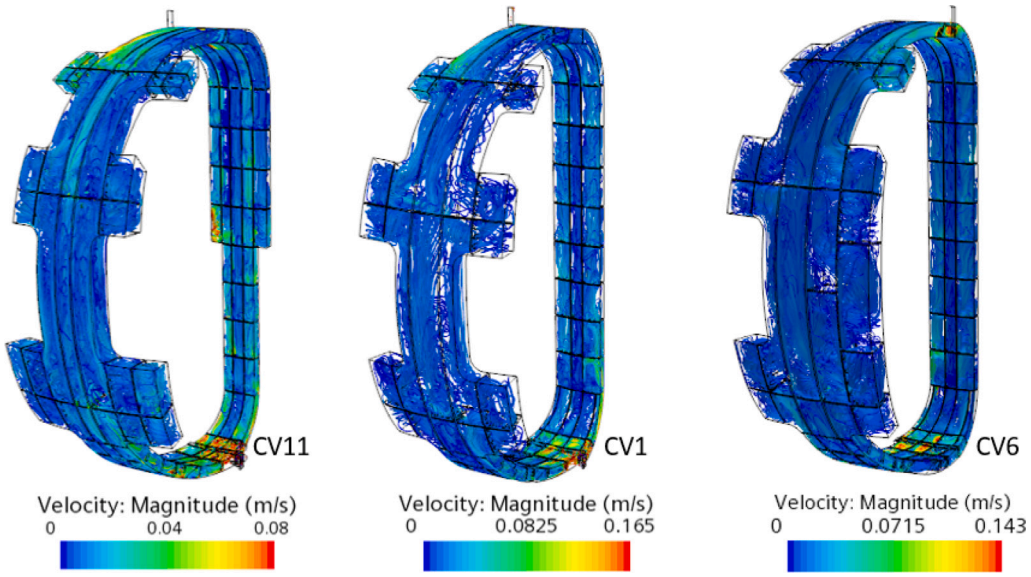

Fig. 10. Streamline visualization for CV11 (special), CV1 (regular) and CV6 (special). The streamlines are generated using as source seed inlet and outlet cross-sections. Info about velocity magnitude is overlapped to obtain a qualitative and quantitative flow field visualization. Velocity magnitude upper bound is cropped at the maximum recorded outside the inlet pipe (where the maximum value of $V = 1.11\ \mathrm{m\,s^{-1}}$ is actually found) to better highlight velocity differences among these CVs.

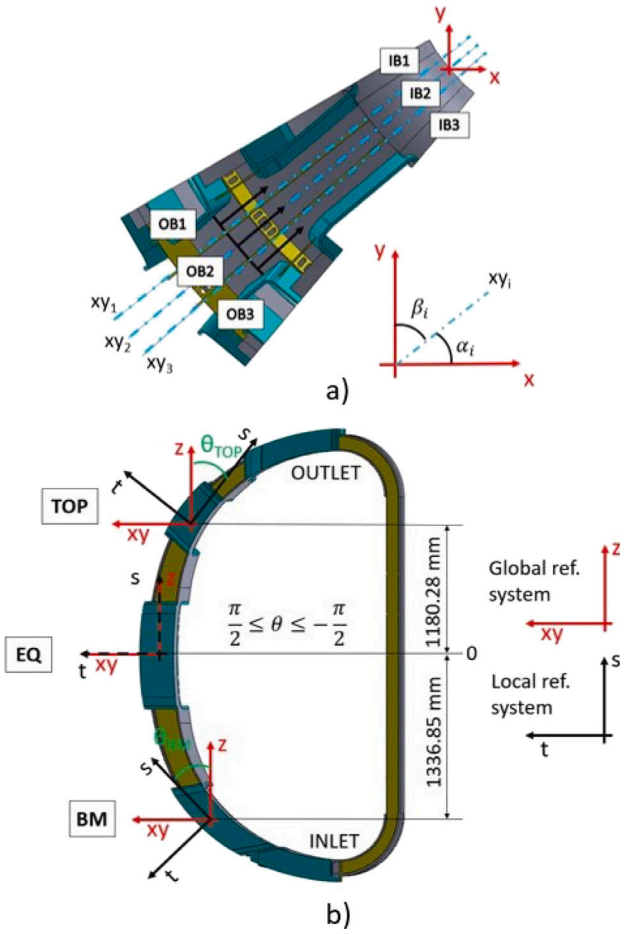

Fig. 11. Visualization of the orientation (a) and latitude (b) of the 18 cross-sections exploited for mass flow rate evaluation in the six OB/IB parallel channels, at three different altitudes: top (TOP), equatorial (EQ) and bottom (BM). While α_i and β_i are different for each CV, $\theta_{BM} = 40.93°$ and $\theta_{TOP} = 45°$ are invariant.

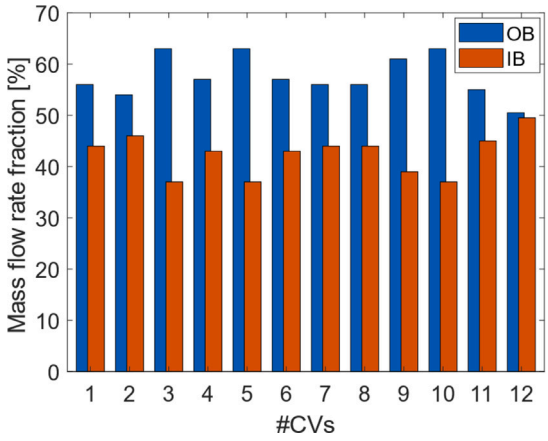

Fig. 12. Mass flow rate repartition (as fraction % of the total prescribed mass flow rate of 1.11 kg/s at the inlet) between IB and OB legs in all the 12 CVs composing the DTT VV.

compared to CFD analyses carried out in the same off-nominal condition: by considering a mass flow rate of 1 $\mathrm{kg\,s^{-1}}$, the deviation between the approximated hydraulic characteristic and high-fidelity CFD results is limited to 0.8%.

In *OpenModelica*, the CV hydraulic characteristic has been included via Flow1DFV objects, with *OpPoint* friction factor specification, which corresponds to solving Eq. (6). In other words, this allows defining the nominal operating point in terms of mass flow rate and pressure drop, and the hydraulic characteristic is assumed to be a parable through that point. From the thermal point of view, the *Ideal Heat Transfer* model is employed to account for a perfect heat transfer between the fluid and the pipe walls (i.e. no thermal gradient across the fluid boundary layer, or infinite heat transfer coefficient), retrieving the global energy balance for each CV, needed to correctly assess the VV outlet mixing temperature. With a *Constant Source Block* (a Modelica block to output a constant quantity) and a *Heat Source* connector (to assign the unit [W] to the constant source), the TS radiative thermal load [W] is prescribed in each pipe (representing a different CV) thermal interface, proportionally to its fluid outer surface. The full VV hydraulic model consists therefore in the parallel connection of the 18 CVs, as shown

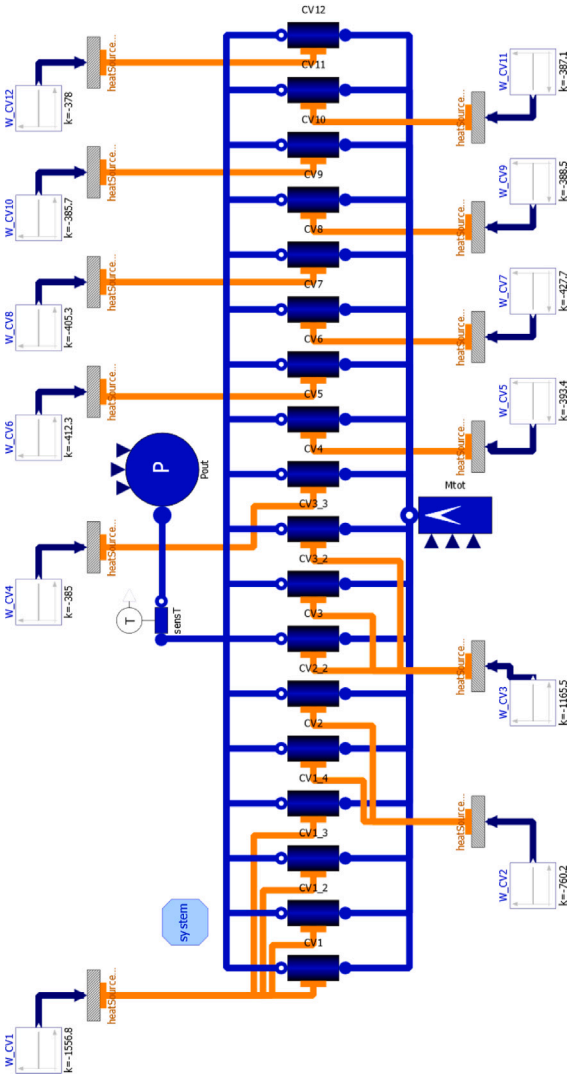

Fig. 13. Complete system-level model of the DTT VV in *OpenModelica*, exploiting the *ThermoPower* library.

in Fig. 13. An inlet mass flow source prescribes the total mass flow of 20 $\mathrm{kg\,s^{-1}}$, while the pressure sink sets the circuit pressure level at ~4 bar, to guarantee a well posed system of non-linear equations. Distinction among 9 staggered inlets and outlets is not accounted for here, but it can be included as soon as information on VV distribution pipes and collector rings will be available.

The results of the VV system-level model are shown in Table 5. Even though they do not take into account the intrinsic transient nature of the solution due to variable pressure drops detected for CV1, CV6, CV7 and CV9, they show the mass flow repartition among the different CVs: the flow unbalance is ± 6%. To properly account for the unsteadiness as well, a 3D unsteady CFD simulation of the entire vacuum vessel is the only option. Moreover, the resulting outlet mixing temperature differs (≈ 0.01 K) from that computed by hand because in the current model thermo-physical properties of standard water are exploited instead those computed for borated water in Section 3.5. To correctly retrieve the real outlet mixing temperature, an ad-hoc Modelica media library must be developed. However, the accuracy of the results is judged to be acceptable for the purpose of computing the mass flow unbalance among the different CVs.

Table 5
Mass flow rate repartition computed by the VV system-level model exploiting pure water thermo-physical properties.

Variable	Value
Δp_{VV} [Pa]	2806.7
$\dot{m}_{CV1}$ [kg s^{-1}]	1.125
$\dot{m}_{CV2}$ [kg s^{-1}]	1.115
$\dot{m}_{CV3}$ [kg s^{-1}]	1.073
$\dot{m}_{CV4}$ [kg s^{-1}]	1.137
$\dot{m}_{CV5}$ [kg s^{-1}]	1.071
$\dot{m}_{CV6}$ [kg s^{-1}]	1.162
$\dot{m}_{CV7}$ [kg s^{-1}]	1.163
$\dot{m}_{CV8}$ [kg s^{-1}]	1.152
$\dot{m}_{CV9}$ [kg s^{-1}]	1.087
$\dot{m}_{CV10}$ [kg s^{-1}]	1.078
$\dot{m}_{CV11}$ [kg s^{-1}]	1.069
$\dot{m}_{CV12}$ [kg s^{-1}]	1.132
T_{mix} [K]	333.062

Regular Special Global

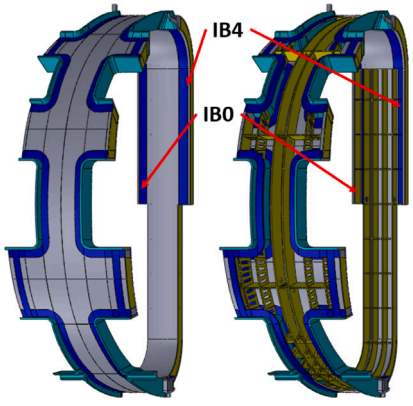

Fig. 14. Geometry of CV11 with (left) and without (right) outer/inner shells. Additional IB channels IB0 and IB4 are highlighted.

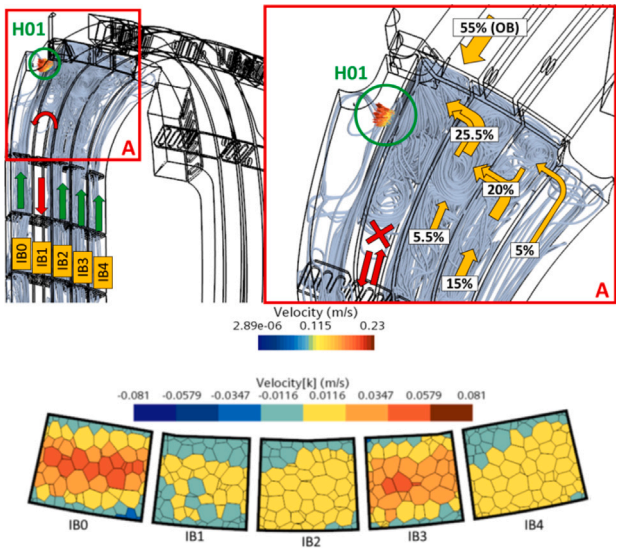

Fig. 15. Visual display of CV11 dynamic fluid plug in IB1 upper region (top). Scalar scenes of V_s velocity distribution at $z = 1180.28$ mm cross-section (bottom).

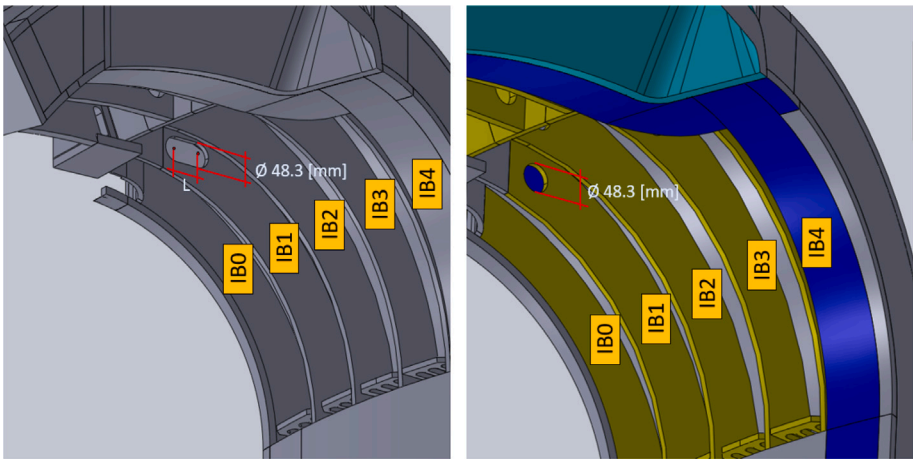

Fig. 16. Original (right) and optimized (left) H01 design.

6. Optimization

In the previous section, it has been anticipated that stagnation/backflow was found in CV11 and CV12. As already stated, they do not represent a significant concern from a thermal-hydraulic point of view. However, a simple but effective strategy to avoid stagnation is suggested to re-distribute the flow of borated water in these two CVs.

6.1. CV11 optimization

Focusing the attention on CV11, the introduction of the additional channels IB0-IB4 at the equatorial level for design integration (see Fig. 14) leads to backflow in the upper region of IB1: once the steady-state is reached, approximately 0.5% of the total mass flow rate slowly circulates in IB1 from top to bottom. The streamlines obtained by integrating backward from the hole H01 (connecting IB0 and IB1 close to the outlet region) reveal that the fluid crossing that hole does not actually come from IB1 channel, while V_s scalar scenes confirms negative velocities (see Fig. 15). This is due to the fact that more than half of the total IB mass flow rate has to be collected and directed towards the outlet pipe through hole H01: the strong recirculation right before it creates a "*dynamic fluid plug*" which hinders the passage of the fluid coming from IB1. The latter is therefore stopped during its way up to the outlet. For that reason, once the steady-state is reached, all the fluid circulating in IB1 shifts to IB0 at the equatorial region while a little fraction of the mass flow rate coming from IB channels IB4, IB3 and IB2 is deflected down to IB1 to then reach the outlet from IB0. That happens because the additional distributed pressure drop related to the passage of the extra mass flow rate $\Delta\dot{m} = 0.5\%\dot{m}_{tot}$ down to IB1 equator and then up in IB0 is still lower than the corresponding localized pressure drop at H01. In IB3 flows 20% of the water in the CV at the bottom, of which 15% proceeds along IB3 up to its top, while only 5% at the equator goes in the additional IB4 channel. This is coherent because the longer fluid path experienced in IB4 (located further from the outlet) has to be balanced by lower fluid velocity to keep the overall pressure drop inside IB3 and IB4 channels equal (in view of the parallel connection). The backflow in the upper region of IB1 does not represent an issue in terms of temperature distribution, but control volume CV11 is characterized by the highest pressure drop (3026 ± 115 Pa).

The proposed optimization consists in changing the shape of that hole, transforming the latter in a buttonhole characterized by the same diameter ($\varnothing = 48.3$ mm) and a width L equal to the diameter itself, as shown in Fig. 16. Therefore, for the same pressure drop (which is imposed by surrounding inboard channels in parallel), more mass flow rate can circulate in IB1. In other words, after the change, the fluid has a less resistive path to pass through H01 instead of going backwards in IB1 to then leave the CV through IB0. The backflow in IB1 channel is thus solved, see the mass flow repartition in IB leg upper region before and after the optimization in Table 6. Moreover, this more uniform flow distribution affects the IB/OB flow repartition as well, which became more balanced, and is accompanied by an overall pressure drop reduction down to $\Delta p = 2887 \pm 115$ Pa (−5%), due to the lower concentrated pressure drops in H01.

The effect of such optimization on structural properties needs to be assessed.

Table 6
Mass flow fraction in CV11 IB upper region before and after the design optimization.

Case	IB0	IB1	IB2	IB3	IB4	TOT
Original	20%	0.5% (<0)	5.5%	15%	5%	45%
Optimized	11.5%	7.5%	7.5%	15%	4.5%	46%

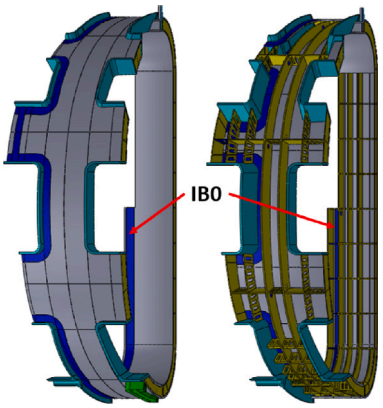

Fig. 17. CV12 geometry.

6.2. CV12 optimization

For CV12 instead the presence of an additional IB channel IB0 at the bottom (from a topology point of view, it is the bottom section of IB4 in CV11, see Fig. 17) introduces reverse flow in the lower region of IB1.

Since this additional IB channel is located at the same side of the inlet pipe, with a buttonhole of the inlet chamber pointing directly to it, the great majority of the coolant will flow in IB0, rather than moving toroidally to the other poloidal paths and then up through IB1. At the

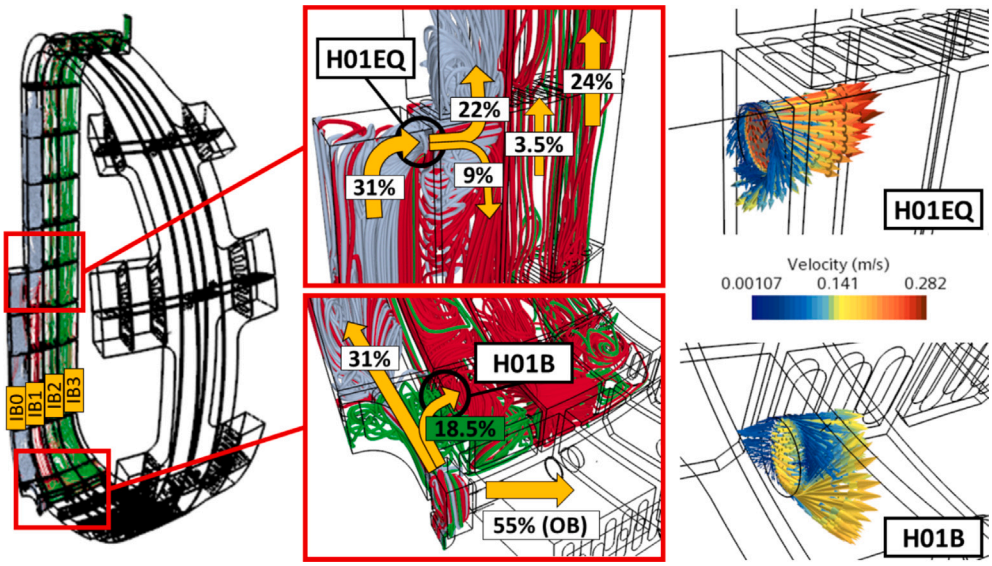

Fig. 18. Flow distribution in CV12, with a focus on inlet and equatorial regions. Green streamlines show the 18.5% of IB mass flow rate flowing in hole H01B reaching IB2 and IB3 channels, while grey/red streamlines indicate the 31% flowing directly in IB0. After hole H01EQ, the grey streamlines (22%) continue in IB1 towards the outlet while the red ones (9%) come back along IB1 to reach IB2/IB3 channels. Streamlines are evaluated on different grids for sake of visualization and therefore they do not provide quantitative information. Vector velocity fields of holes H01B and H01EQ are reported as well (right) to show the velocity magnitude and of the overall flow direction.

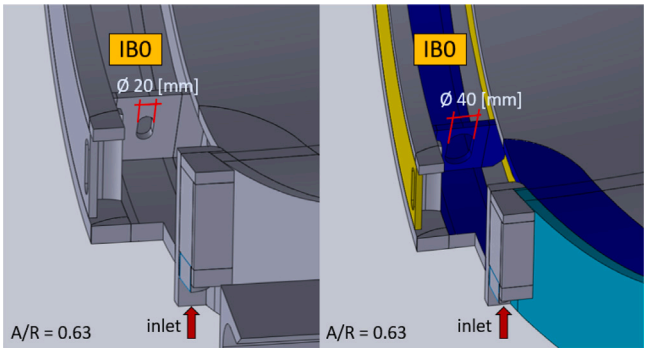

Fig. 19. Updated design of IB0 buttonhole (left) with respect to the original one (right).

equatorial level, IB0 mass flow rate (31% of the total one) converges into IB1: 22% flows up in IB1, while the remaining 9% flows down to the bottom of IB1 to be then re-distributed between IB2 and IB3 channels, as shown in Fig. 18.

Despite the backflow at the bottom of IB1, the TH results confirm that also for CV12 no relevant issues are found in terms of pressure drop, minimum temperature and overall flow repartition between IB/OB branches. However, a more equally distributed coolant repartition can be achieved by acting on the size of the IB0 buttonhole. By keeping the original aspect ratio $R/L = 0.63$, the buttonhole radius has been reduced from $R = 20$ mm in the original design, to an optimized value of $R = 10$ mm, as shown in Fig. 19. For manufacturing purposes, a simple hole sharing the same diameter can be adopted as well. Therefore, the fluid finds a less resistive path to flow through H01B and then proceed up inside IB1.

This solves the backflow in IB1: Table 7 presents the updated flow repartition in the bottom region of the CV12 IB. The proposed design modification is conservative in terms of structural properties (which is preferred, since the bottom of the VV should provide support to the divertor rail), but on the other hand by partially occluding the fluid passage, this CV's pressure drop increases up to 2776 ± 115 Pa (+3%).

After the optimization the IB mass flow rate becomes larger than the OB one (50.5%, 49.5% respectively).

Table 7
Mass flow repartition in the bottom region of CV12 IB before and after the proposed design optimization.

Case	IB0	IB1	IB2	IB3	TOT
Original	31%	9% (<0)	3.5%	24%	49.5%
Optimized	20%	4%	1.5%	25%	50.5%

7. Conclusions and perspective

In this work, the thermal-hydraulic characterization of the DTT VV is carried out by means of high-fidelity CFD analyses. The results are based on three *modelling assumptions*:

I Neglect existing pressure coupling between adjacent CVs sharing the same inlet or outlet.
II Model, discretize and solve equations for the fluid volume only (no conjugate heat transfer). This is a conservative approach since hot/cold spots are not dumped by thermal diffusion in the solid.
III Assume homogeneous mass flow repartition among the 9 inlets ($2.22\ \mathrm{kg\,s^{-1}}$) and in turn in the adjacent CVs ($1.11\ \mathrm{kg\,s^{-1}}$); hypothesis that is verified a posteriori with a system-level model (see Section 5).

allowing a separate characterization of the 12 different types of CVs (*Regular* and *Special*) into which the DTT VV can be subdivided for what regards the coolant macroscopical flow paths. Detailed model explorations on regular CV1 allowed to define the best compromises between accuracy of the solution and computational cost in the mesh definition, and to assess the non negligible effect of natural convective flows. The resulting momentum-energy coupling was addressed with the Boussinesq approximation in view of the limited temperature variations in the computational domain, while the turbulent nature of the flow in some regions was approached with the SST $k-\omega$ turbulence closure.

The most relevant results are:

1. From a numerical point of view, due to the complexity of the fluid geometry the steady solver is not always able to find a clean solution. However, it has been demonstrated that it is

able to predict average values of the thermal-fluid dynamic variables where global relevant quantities are sufficiently in agreement with those retrieved from more refined meshes with the unsteady solver.
2. Each of the 12 temperature distributions fall safely in the desired temperature range. The VV outlet temperature resulting from the adiabatic mixing of the borated water coming from the 9 outlets is $T_{out,mix} = 333.06$ K.
3. The pressure drop of each CV, being it "Special" or "Regular", is within the range $2561 \div 3026$ Pa. The overall VV pressure drop (system-level model) is estimated to be of 2810 Pa.
4. Peculiar IB channel topologies in CV11 and CV12 introduce stagnation and backflow in portions of the IB channels, which can be solved by modifying the shape/dimension of already existing apertures to tune the hydraulic resistance of each channel, thus reducing the stagnation issues.

Important simplifications have been made also for what regards the thermal load acting on the VV, neglecting the pulsed nuclear loads and positive heat fluxes coming from the divertor in view of the low energy deposited during the short plasma duration, if compared with the steady state heat flux subtracted by the thermal shield. In future transient simulations they will be included as well, together with the solid domain to account for its thermal inertia. The system-level model developed in this work will also be used to simulate accidental transients in the VV, such as loss-of-flow and loss-of-coolant. A full 3D, unsteady CFD simulation of the entire VV (≈ 400 million cells expected if the finest mesh is adopted) to study separately the effect of outlet and inlet coupling by imposing target mass flow-rate boundary conditions at the outlet can also represent a reference to verify the system-level model approximation presented here to assess the mass flow repartition among the different CVs.

CRediT authorship contribution statement

Roberto Bonifetto: Writing – review & editing, Supervision, Resources, Methodology, Conceptualization. **Gianluca Barone:** Project administration. **Mauro Dalla Palma:** Project administration, Funding acquisition. **Antonio Froio:** Writing – review & editing, Supervision, Resources, Methodology. **Emanuela Martelli:** Project administration. **Federico Vair:** Writing – original draft, Visualization, Software, Methodology, Investigation, Data curation. **Roberto Zanino:** Supervision, Resources. **Andrea Zappatore:** Writing – review & editing, Supervision, Methodology.

Declaration of competing interest

The authors declare that they have no known competing financial interests or personal relationships that could have appeared to influence the work reported in this paper.

Data availability

No data was used for the research described in the article.

Acknowledgements

This work has been carried out within the framework of the EUROfusion Consortium, funded by the European Union via the Euratom Research and Training Programme (Grant Agreement No 101052200 – EUROfusion). Views and opinions expressed are however those of the author(s) only and do not necessarily reflect those of the European Union or the European Commission. Neither the European Union nor the European Commission can be held responsible for them. The work of AZ is financially supported by a EUROfusion Researcher Grant.

Computational resources were provided by HPC@POLITO, a project of Academic Computing within the Department of Control and Computer Engineering at the Politecnico di Torino (http://www.hpc.polito.it).

References

[1] A.J.H. Donné, W. Morris, X. Litaudon, C. Hidalgo, D. McDonald, H. Zohm, E. Diegele, A. Möslang, K. Nordlund, G. Federici, European research roadmap to the realization of fusion energy eurofusion consortium, 2018.
[2] T. Eich, A.W. Leonard, R.A. Pitts, W. Fundamenski, R.J. Goldston, T.K. Gray, A. Herrmann, A. Kirk, A. Kallenbach, O. Kardaun, et al., Scaling of the tokamak near the scrape-off layer H-mode power width and implications for ITER, Nucl. Fusion 53 (2013) 093031.
[3] R. Ambrosino, et al., DTT-divertor Tokamak test facility: A testbed for DEMO, Fusion Eng. Des. 167 (2021) 112330.
[4] G. Mazzitelli, R. Albanese, F. Crisanti, P. Martin, A. Pizzuto, A.A. Tuccillo, R. Ambrosino, A. Appi, G. Di Gironimo, A. Di Zenobio, et al., Role of Italian DTT in the power exhaust implementation strategy, Fusion Eng. Des. 146 (2019) 932–936.
[5] ENEA, Divertor Tokamak test facility interim design report — A milestone along the roadmap to the realisation of fusion energy, 2019, URL https://www.dtt-project.it/index.php/dtt-green-book.html.
[6] R. Ambrosino, A. Castaldo, DTT reference PF scenarios, issue 1,8 may 2020. Internal DTT report, 2020.
[7] Siemens, Simcenter STAR-ccm+ software, 2023, URL https://plm.sw.siemens.com/it-IT/simcenter/fluids-thermal-simulation/star-ccm/.
[8] F.R. Menter, Two-equation eddy-viscosity turbulence models for engineering applications, AIAA J. 32 (1994) 1598–1605.
[9] Siemens, Simcenter STAR-ccm+: User guide, 2022.
[10] R. Villari, M. Angelone, B. Caiffi, A. Colangeli, F. Crisanti, D. Flammini, N. Fonnesu, R. Luis, G. Mariano, D. Marocco, et al., Nuclear design of divertor tokamak test (DTT) facility, Fusion Eng. Des. 155 (2020) 111551.
[11] C. Gasparrini, D. Badocco, L. Di Pace, N. Terranova, P. Pastore, F. Montagner, L. Mattarozzi, R. Villari, E. Martelli, S. Roccella, et al., Water chemistry in fusion cooling systems: Borated water for DTT vacuum vessel, IEEE Trans. Plasma Sci. (2022).
[12] A.V. Morozov, A.V. Pityk, A.R. Sahipgareev, A.S. Shlepkin, Experimental study of the thermophysical properties of boric acid solutions at the parameters typical of the WWER emergency mode, in: Journal of Physics: Conference Series, vol. 1128, IOP Publishing, 2018, 012103.
[13] M. He, C. Su, X. Liu, X. Qi, Isobaric heat capacity of boric acid solution, J. Chem. Eng. Data 59 (2014) 4200–4204.
[14] N.K. Çakmak, Experimental study of thermal conductivity of boric acid–water solutions, Heat Transfer Res. 50 (2019).
[15] L. Savoldi Richard, R. Bonifetto, R. Zanino, S. Corpino, G. Obiols-Rabasa, J. Izquierdo, R. Le Barbier, Y. Utin, CFD analysis of a regular sector of the ITER vacuum vessel. Part I: Flow distribution and pressure drop, Fusion Eng. Des. 88 (2013) 3272–3279.
[16] R. Zanino, L. Savoldi Richard, F. Subba, S. Corpino, J. Izquierdo, R. Le Barbier, Y. Utin, CFD analysis of a regular sector of the ITER vacuum vessel. Part II: Thermal-hydraulic effects of the nuclear heat load, Fusion Eng. Des. 88 (2013) 3248–3262.
[17] F. Casella, A. Leva, et al., Modelica open library for power plant simulation: Design and experimental validation, in: Proceeding of the 2003 Modelica Conference, Linkoping, Sweden, Citeseer, 2003.
[18] F. Casella, A. Leva, Modelling of thermo-hydraulic power generation processes using modelica, Math. Comput. Model. Dyn. Syst. 12 (2006) 19–33.